

Fisher-Based Sensitivity Framework for Rydberg Atom Microwave Electrometry

Chen-Rong Liu,^{1,*} Runxia Tao,^{1,*} Xiang Lv,² Ying Dong,¹ Chuang Li,^{1,†} Binbin Wei,^{3,‡} and Mingti Zhou^{1,§}

¹College of Metrology Measurement and Instrument,
China Jiliang University, Hangzhou, 310018 China

²Department of Physics, Westlake University, Hangzhou, 310030 China

³Qianyuan Laboratory, Xihu District, Hangzhou, Zhejiang Province, 310024 China
(Dated: March 4, 2026)

Fisher information provides a rigorous theoretical benchmark for evaluating quantum sensor sensitivity; however, a comprehensive framework for quantifying the fundamental limits of Rydberg-atom microwave electrometers remains lacking. In this work, we establish such a framework by deriving the Fisher information for slope detection and establishing its connection to sensitivity through signal-to-noise ratio, leading to an analytical expression jointly determined by photon shot noise and atomic response. Numerical implementation with real parameters in cesium vapor systems reveals a Fisher-optimized sensitivity below $\text{nV cm}^{-1} \text{Hz}^{-1/2}$, highlighting a substantial potential for sensitivity enhancement in practical experiments through the suppression of technical noise. Importantly, the theory predicts that sub-nanovolt sensitivity is robust against moderate variations in system parameters, thereby delineating both the ultimate sensitivity and optimal operational regime of Rydberg-atom microwave electrometers.

I. INTRODUCTION

Rydberg atoms exhibit exaggerated atomic properties, such as the scaling of dipole-dipole interactions as n^4 and the scaling of radiative lifetime as n^3 with the principal quantum number n , making them a current research hotspot in quantum information, quantum computing, and quantum precision measurement [1–6]. In recent years, Rydberg-atom microwave electrometers (RAME) have demonstrated remarkable sensitivity by leveraging electromagnetically induced transparency (EIT) and Autler-Townes (AT) splitting phenomena [7, 8]. The core detection mechanism relies on measuring the AT splitting interval in EIT spectra, such that $\Delta_{\text{AT}} \propto \Omega_s$ [8, 9]. This EIT-AT-based approach has led to significant advances [9–16], achieving sensitivities on the order of $\mu\text{V cm}^{-1} \text{Hz}^{-1/2}$ in room-temperature atomic vapor cells [17, 18]. A major breakthrough came with the introduction of the atomic superheterodyne detection scheme by Jing *et al.*, which achieved a three-orders-of-magnitude improvement in sensitivity— $55 \text{ nV cm}^{-1} \text{Hz}^{-1/2}$ at room temperature [19], and $10 \text{ nV cm}^{-1} \text{Hz}^{-1/2}$ at $200 \mu\text{K}$ [20]—surpassing traditional EIT-AT protocols. This performance is comparable to that of many-body Rydberg criticality metrology, which has demonstrated sensitivity levels of $49 \text{ nV cm}^{-1} \text{Hz}^{-1/2}$ [21], offering yet another promising route for high-precision microwave sensing. Moreover, cavity-enhanced strategies [22, 23] that integrate many-body criticality effects [24] show potential for pushing sensitivities further into the sub-nV $\text{cm}^{-1} \text{Hz}^{-1/2}$ regime.

The many-body Rydberg criticality and atomic superheterodyne techniques represent paradigm shifts from conventional EIT-AT-based strategies. The former harnesses enhanced susceptibility near quantum critical points, while the latter is based on slope detection [25]. Notably, despite their differing physical principles, both approaches enhance sensitivity through a common mechanism—by utilizing the gradient or slope of spectroscopic signals. In slope detection, the sensor response is linearized by evaluating the derivative $\partial X/\partial \xi$ of a measurable observable X with respect to the parameter of interest ξ , at an optimal working point ξ_0 [25]. This enables the detection of small variations ($\delta \xi \ll \xi_0$) through the linear approximation $\delta X \approx (\partial X/\partial \xi)\delta \xi$. The ultimate limit of precision in parameter estimation is governed by the Fisher information $F(\xi)$, as constrained by the Cramér–Rao bound $\text{Var}(\xi) \geq 1/F(\xi)$ [26–28].

While Fisher information has been extensively applied in quantum metrology [25], its systematic adaptation to RAME—especially in optimizing sensitivity—remains underdeveloped. Two theoretical gaps are particularly identified: (i) the absence of a generalized Fisher information formulation specific to slope detection in RAME, and (ii) the lack of a quantitative relationship between conventional sensitivity metrics and $F(\xi)$. Addressing these gaps is further complicated by RAME’s indirect measurement architecture, where quantum noise [29] and atomic relaxation dynamics simultaneously affect probe transmission signals, making it challenging to disentangle their respective contributions to sensitivity limitations.

In this work, we systematically applies Fisher information formalism to slope detection in RAME, establishing a universal framework for determining the theoretical sensitivity benchmark under ideal, shot-noise-limited conditions. Recognizing the pivotal role of signal-to-noise ratio (SNR) in determining measurement sensitivity, we analytically relate SNR to Fisher information via error propagation and parameter estimation theory. Our

* These authors contributed equally to this work.

† chuangli@cjlu.edu.cn

‡ weibb.2009@tsinghua.org.cn

§ mtchou@cjlu.edu.cn

analysis elucidates how measurement uncertainty arises from quantum fluctuations in the transmitted probe laser power, while atomic relaxation processes govern the overall attenuation of the probe signal (Fig. 1). This provides a physical explanation for the sensitivity enhancement observed in atomic superheterodyne detection [19]. Building upon this general framework, we further perform numerical studies specific to cesium Rydberg-atom systems, identifying critical operating regimes where sensitivity sustains the sub-nV cm⁻¹ Hz^{-1/2} level, jointly limited by optical shot noise and atomic response. The corresponding experimental configuration, illustrated in Fig. 1, employs atomic vapor cell transmission spectroscopy ($P_{\text{in}} \rightarrow P_{\text{tr}}$) to detect the microwave-induced linearized power response.

The remainder of this manuscript is organized as follows: Section II derives the Fisher information expression and sensitivity limits via error propagation, and formulates general criteria for sensitivity optimization. Section III applies the framework to cesium-based Rydberg systems, demonstrating shot-noise-limited performance and evaluating robustness across parameter regimes. A detailed discussion and concluding remarks are provided in Section IV.

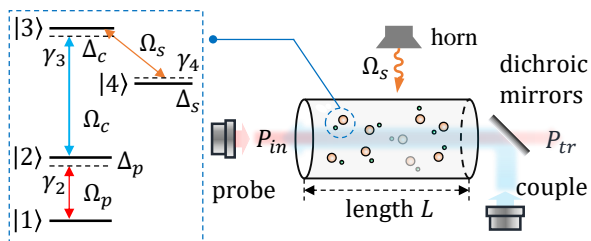


FIG. 1. (Color online) **A schematic of RAME.** Probe laser (input power P_{in}) propagates through a vapor cell (length L), with transmitted power P_{tr} . Microwave field (Rabi frequency Ω_s) introduced via horn antenna [9]. Corresponding four-level atomic system configuration is detailed in Table I.

II. THEORETICAL FRAMEWORK OF FISHER INFORMATION AND SENSITIVITY

In this section, we systematically present our theoretical framework to evaluate the RAME performance. Firstly, we present the basic conversion of microwave-to-optical transduction via slope detection. After that, we derive the Fisher information through error propagation analysis and double check with that via parameter estimates. Finally, we derive the sensitivity limits via signal-to-noise ratio (SNR) of the transmitted probe power, and rigorously connect these two metrics, demonstrating how Fisher information maximization enables identification of optimal operating conditions for RAME.

A. Slope Detection Principle

The operational schematic of RAME based on slope detection is illustrated in Fig. 1. The core apparatus is an atomic vapor cell, which can be treated as a linear medium [9, 30] at room temperature for the counterpropagating probe and coupling laser.

The incident (P_{in}) and transmitted (P_{tr}) probe laser powers exhibit a microwave-dependent transmission governed by:

$$P_{\text{tr}} = P_{\text{in}} \cdot \eta(\Omega_s), \quad (1)$$

where $\eta(\Omega_s)$ quantifies the probe attenuation through the atomic medium as a function of the microwave Rabi frequency Ω_s . This attenuation is governed by the Beer-Lambert law:

$$\eta(\Omega_s) = \exp \left\{ -\frac{2\pi L}{\lambda_p} \text{Im} [\chi(\Omega_s)] \right\}, \quad (2)$$

with $\chi(\Omega_s)$ being the complex susceptibility that originates from the microwave-modulated atomic polarization of probe laser transmission [31, 32], and λ_p the probe laser wavelength. Explicitly, $\chi(\Omega_s)$ depends on the density matrix element ρ_{21} :

$$\chi(\Omega_s) = -\frac{2\mathcal{N}_0\mu_{21}^2}{\epsilon_0\hbar\Omega_p}\rho_{21}, \quad (3)$$

where \mathcal{N}_0 is the atomic vapor density (m⁻³) calculated via the Clausius-Clapeyron equation [30], μ_{21} denotes the dipole matrix element for the $|1\rangle \rightarrow |2\rangle$ transition (Fig. 1), Ω_p is the probe Rabi frequency, ϵ_0 is the vacuum permittivity, and \hbar is the reduced Planck constant.

The density matrix element ρ_{21} in rotating frame [32] is obtained by solving the quantum master equation under steady-state conditions ($\partial\rho/\partial t = 0$):

$$\frac{\partial\rho}{\partial t} = \frac{1}{i\hbar}[H, \rho] + \mathcal{L}\rho, \quad (4)$$

where H is the Hamiltonian and ρ denotes the density matrix. The term $\mathcal{L}\rho$ captures atomic relaxations, including: (1) population decay driven by spontaneous emission [32] and environmental thermal radiation [33], and power broadening due to laser saturation [32] which is incorporated within the decay formalism since it directly modifies effective transition rates; (2) dephasing due to atom-atom collisions [34–36], transit-time broadening [37, 38], laser linewidth [17, 35, 39], and Doppler effect [35, 39]. Detailed mechanisms of relevant relaxation supporting derivations and analysis are presented in the Supplemental Material[40] (see also references [41–47]). Solving this master equation yields the probe light transmission $\eta(\Omega_s)$ as the core observable. This quantity directly links the microscopic atomic dynamics, driven by the microwave field Ω_s to the experimentally measurable macroscopic signal.

C. The Limited Sensitivity

The SNR serves as the fundamental metric for quantifying the sensitivity of RAME. Following quantum metrology conventions [25], we express the SNR as the ratio of microwave-induced power variation δP_{tr} to intrinsic quantum power fluctuations $\sigma_{P_{\text{tr}}}$:

$$\text{SNR} = \frac{\delta P_{\text{tr}}}{\sigma_{P_{\text{tr}}}} = \frac{\delta \Omega_s}{\sigma_{\Omega_s}}, \quad (15)$$

where the SNR of microwave Ω_s to be measured inherits from the detection chain described in Eq. (5), including error propagation in Eq. (11). The minimum detectable microwave perturbation $\delta \Omega_s$, defined at $\text{SNR}=1$ and bounded by the Cramér-Rao inequality [26], is determined through the Fisher information $F(\Omega_s)$ [Eq. (14)] as:

$$[\delta \Omega_s]_{\min} = \sigma_{\Omega_s} = \frac{1}{\sqrt{F(\Omega_s)}}. \quad (16)$$

Adopt the standard quantum sensing framework with normalized integration time ($T = 1$ s) [25], we obtain the fundamental sensitivity limit:

$$\mathcal{E}_s = \frac{\hbar}{\mu_s} [\delta \Omega_s]_{\min} \cdot \sqrt{T} = \frac{\hbar}{\mu_s} \sqrt{\frac{T}{F(\Omega_s)}}. \quad (17)$$

This expression is intrinsically independent of integration time due to the reciprocal time-scaling relationships in Eqs. (10) and (14), consistently producing sensitivities in the standard metrological units of $\text{V m}^{-1} \text{Hz}^{-1/2}$. This formulation demonstrates how Fisher information fundamentally governs the ultimate sensitivity limit and dictates its optimization.

The standard quantum limit (SQL) [56] is consequently recovered in our formalism through

$$E_{\text{SQL}} = \frac{\mathcal{E}_s}{\sqrt{T}} = \frac{\hbar}{\mu_s \sqrt{N_{\text{in}}}} \frac{1}{|\partial \ln \eta / \partial \Omega_0|}, \quad (18)$$

revealing two distinct scaling dependencies: (i) shot noise governed by photon statistics $\propto 1/\sqrt{N_{\text{in}}}$, and (ii) atomic response determined by microwave-modulated transmission variations $\propto 1/|\partial \ln \eta / \partial \Omega_0|$.

In slope detection, one might naively assume that optimal sensitivity is achieved by simply maximizing the slope κ_p . However, as shown in Eq. (11), the atomic dynamics—characterized by $\eta(\Omega_s)$ —also contribute to the noise floor. Therefore, it is crucial to emphasize that maximizing the Fisher information, rather than the slope alone, is essential for determining the optimal experimental parameters to achieve the best sensitivity.

III. NUMERICAL IMPLEMENTATION

With explicit expressions for Fisher information and sensitivity at hand, we can now identify the optimal experimental parameters by maximizing Fisher information.

A. Atomic Relaxations

In the RAME slope detection scheme, the transmitted probe power depends not only on photon shot noise but also on the atomic response. Therefore, it is crucial to rigorously analyze the various atomic relaxation mechanisms in a quantitative manner. Atomic relaxation mechanisms in RAME can be classified into two distinct categories as previously stated: (i) *decay mechanisms* including spontaneous emission [32], environmental thermal radiation [33], and laser power broadening [32] that alter population distributions among energy levels; and (ii) *dephasing mechanisms* involving atom-atom collisions [34], and Doppler effects [35, 39] that disrupt quantum coherence while preserving population distributions [32]. Experimentally, however, transit-time broadening can be suppressed by enlarging the beam waist radius w_0 [19, 37, 38]), and the laser linewidth can be reduced to hertz (Hz) or even millihertz (mHz) levels using advanced frequency stabilization techniques [57–60]. It is therefore justified to adopt an idealized model that neglects transit-time and laser linewidth dephasing. This idealized framework deliberately sets aside the dominant frequency-to-amplitude noise conversion of laser phase noise encountered in practical experiments (analyzed in Supplemental Material [40] and Fig. 2). It thereby enables us to isolate and analyze the Fisher information under ideal shot-noise-limited conditions, establishing a clear theoretical benchmark for experimental optimization.

Under the rotating-wave approximation (RWA), the rotating-frame Hamiltonian takes the matrix form:

$$H = \frac{\hbar}{2} \begin{bmatrix} 0 & \Omega_p & 0 & 0 \\ \Omega_p & -2\Delta_p & \Omega_c & 0 \\ 0 & \Omega_c & -2(\Delta_p + \Delta_c) & \Omega_s \\ 0 & 0 & \Omega_s & -2(\Delta_p + \Delta_c - \Delta_s) \end{bmatrix}, \quad (19)$$

where Ω_p , Ω_c , and Ω_s denote probe, coupling, and microwave Rabi frequencies, respectively. The detuning parameters are defined through atomic transition frequencies [19]:

$$\begin{aligned} \Delta_p &= \omega_1 + \omega_p - \omega_2, \\ \Delta_c &= \omega_2 + \omega_c - \omega_3, \\ \Delta_s &= \omega_4 + \omega_s - \omega_3, \end{aligned}$$

as illustrated in Fig. 1.

For warm atomic vapor, the Lindblad operator describing decay processes is:

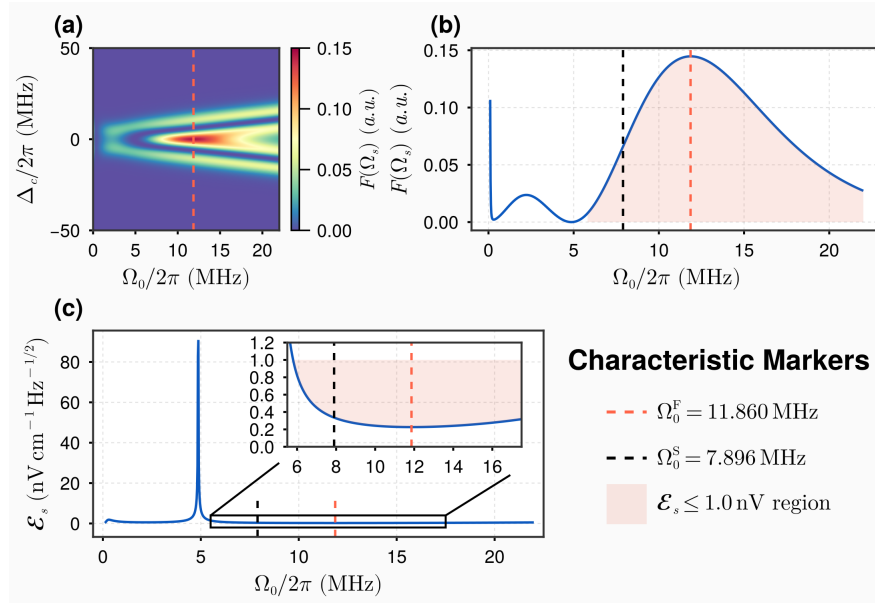


FIG. 2. (Color online) **Sub-nV Sensitivity in a Robust Operational Window.** (a) Heatmap of Fisher information $F(\Omega_s)$ [Eq. (14)] versus reference microwave Rabi frequency Ω_0 and coupling detuning Δ_c , under $\Delta_p = \Delta_s = 0$. (b) comparison of two characteristic operation points at $\Delta_c = 0$ with vertical lines marking: Fisher information maximum at $\Omega_0^F/2\pi = 11.860$ MHz (dashed orange), and local microwave Rabi frequency $\Omega_0^S/2\pi = 7.896$ MHz (dashed black) in Ref. 19. (c) Microwave field measurement sensitivity \mathcal{E}_s [Eq. (17)] versus Ω_0 at $\Delta_c = 0$ demonstrates a continuous operational regime (shaded region in (b,c) with a wide range of reference microwave Rabi frequency $\Omega_0/2\pi \sim [5, 30]$ MHz) maintaining shot-noise-limited sub-nV sensitivity ($\mathcal{E}_s \leq 1.0$ nV cm $^{-1}$ Hz $^{-1/2}$), with optimal performance $\mathcal{E}_s^{\text{opt}} = 0.227$ nV cm $^{-1}$ Hz $^{-1/2}$ (dashed orange vertical line). The legend for vertical lines in subplot (c) and its inset (identical to those in panels (b)) is positioned on the right side of (c). All parameters listed in Table I replicate the experimental parameters from Ref. 19.

$$\mathcal{L}_{\text{decay}}\rho = \begin{bmatrix} \gamma_2\rho_{22} + \gamma_4\rho_{44} & -\frac{\gamma_2}{2}\rho_{12} & -\frac{\gamma_3}{2}\rho_{13} & -\frac{\gamma_4}{2}\rho_{14} \\ -\frac{\gamma_2}{2}\rho_{21} & \gamma_3\rho_{33} - \gamma_2\rho_{22} & -\frac{\gamma_2 + \gamma_3}{2}\rho_{23} & -\frac{\gamma_2 + \gamma_4}{2}\rho_{24} \\ -\frac{\gamma_3}{2}\rho_{31} & -\frac{\gamma_3 + \gamma_2}{2}\rho_{32} & -\gamma_3\rho_{33} & -\frac{\gamma_3 + \gamma_4}{2}\rho_{34} \\ -\frac{\gamma_4}{2}\rho_{41} & -\frac{\gamma_4 + \gamma_2}{2}\rho_{42} & -\frac{\gamma_4 + \gamma_3}{2}\rho_{43} & -\gamma_4\rho_{44} \end{bmatrix}, \quad (20)$$

where γ_2 , γ_3 , and γ_4 denote effective decay rates for transition $|2\rangle \rightarrow |1\rangle$, $|3\rangle \rightarrow |2\rangle$, and $|4\rangle \rightarrow |1\rangle$ respectively, that can be calculated using Alkali Rydberg Calculator [33].

The dominant collision-induced dephasing primarily arises from Rydberg-ground state atomic collision [34, 36, 61, 62], incorporating both elastic and inelastic collisions. This dephasing mechanism is described by the Lindblad operator:

$$\mathcal{L}_{\text{deph}}\rho = \begin{bmatrix} 0 & 0 & -\Gamma_{c3}\rho_{13} & -\Gamma_{c4}\rho_{14} \\ 0 & 0 & 0 & 0 \\ -\Gamma_{c3}\rho_{31} & 0 & 0 & 0 \\ -\Gamma_{c4}\rho_{41} & 0 & 0 & 0 \end{bmatrix}, \quad (21)$$

with Γ_{c3} and Γ_{c4} as collision-induced dephasing rates for the $|3\rangle \rightarrow |1\rangle$ and $|4\rangle \rightarrow |1\rangle$, respectively [62].

The total dissipation combines these effects:

$$\mathcal{L}\rho = \mathcal{L}_{\text{decay}}\rho + \mathcal{L}_{\text{deph}}\rho.$$

Additionally, probe-induced power broadening alters the

$|2\rangle \rightarrow |1\rangle$ transition rate via saturated absorption effects [32], while Doppler broadening is modeled through Boltzmann-weighted averaging of the coherence term ρ_{21} [39]. Detailed derivations are provided in the Supplemental Material [40].

B. Operational Window of Reference Microwave Rabi Frequency

Our framework enables the systematic optimization of microwave-field measurement sensitivity through Fisher information maximization. This maximization involves locating the zeros of the first derivative of the Fisher information F_s with respect to the reference Rabi frequency Ω_0 :

$$\frac{\partial F(\Omega_s)}{\partial \Omega_0} = 2N_{\text{in}} \frac{\partial \ln \eta}{\partial \Omega_0} \left[- \left(\frac{\partial \ln \eta}{\partial \Omega_0} \right)^2 + \frac{1}{\eta} \frac{\partial^2 \eta}{\partial \Omega_0^2} \right] = 0, \quad (22)$$

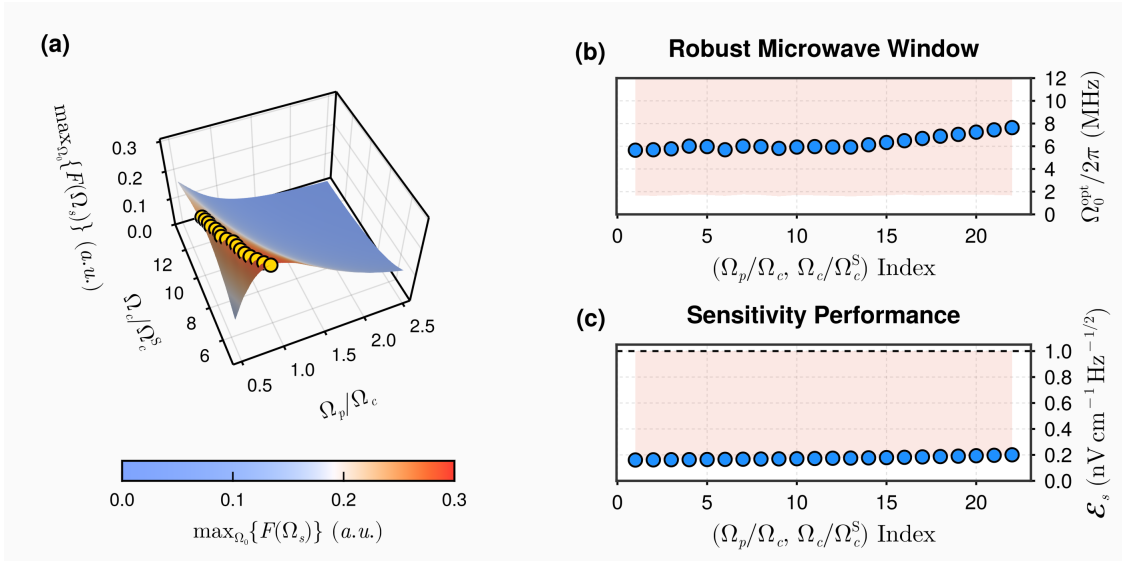


FIG. 3. (Color online) **Universal Optimization of Microwave Sensing Parameters.** (a) 3D surface of Fisher information $\max_{\Omega_0} \{F(\Omega_s)\}$ maximized over reference microwave Ω_0 , mapped as functions of probe-to-coupling ratio Ω_p/Ω_c and normalized coupling strength Ω_c/Ω_c^S under three-photon resonance ($\Delta_p = \Delta_s = \Delta_c = 0$). Gold circle marks local maxima along the ridge suggests optimal $(\Omega_p, \Omega_c, \Omega_0)$ configurations. (b,c) Parameter-optimized characteristics along the ridge in (a): optimal reference microwave Rabi frequency Ω_0^{opt} and corresponding sensitivity $\mathcal{E}_s^{\text{opt}}$, respectively. Shading band indicates robust operational window sustaining sub-nV sensitivity $\mathcal{E}_s^{\text{opt}} \leq \mathcal{E}_s \leq 1.0 \text{ nV cm}^{-1} \text{ Hz}^{-1/2}$ as in Fig. 2(b,c). All configurations along the ridge in (a) achieve $\mathcal{E}_s^{\text{opt}} < 1.0 \text{ nV cm}^{-1} \text{ Hz}^{-1/2}$.

IV. CONCLUSION

The application of a Fisher-information framework enables a rigorous determination of the fundamental sensitivity limits in RAME under slope detection protocols. By integrating parameter estimation theory with error propagation analysis, we identify Fisher information as the key metric governing measurement precision and explicitly relate it to the signal-to-noise ratio of the transmitted probe light. Our analysis reveals that the ultimate sensitivity is constrained by two primary factors: (1) optical shot noise, scaling as $1/\sqrt{N_{\text{in}}}$, arising from photon statistics, and (2) microwave-encoded atomic nonlinear response in the probe transmission, captured by the derivative $\partial \ln \eta / \partial \Omega_0$. Crucially, we clarify that the noise floor is determined by optical intensity detection of the transmitted probe power—rather than direct atomic state projection—with the fundamental limit set by the quantum statistics of light (shot noise), despite of both noise types being formally consistent with the standard quantum limit.

Therefore, it is crucial to distinguish the purpose of our framework from how it should be interpreted. While our analysis provides the fundamental sensitivity limit under the stated idealizations, any practical system will be affected by additional technical noise. The large discrepancy between our prediction and experimental results does not stem from a failure of the model but rather validates its utility as a benchmark: it clearly demonstrates that the primary path to bridging this gap lies

in the meticulous suppression of classical noise sources, most notably laser frequency noise, to approach the shot-noise-limited regime.

To validate our framework, numerical implementation using cesium-133 parameters from Ref. 19 predict a sensitivity limit of $0.227 \text{ nV cm}^{-1} \text{ Hz}^{-1/2}$, substantially surpassing existing experimental records ($55 \text{ nV cm}^{-1} \text{ Hz}^{-1/2}$), quantifying the substantial potential for enhancement available through the suppression of technical noise. Additionally, our numerical results reveal robustness near the optimal operating point: significant deviations in probe-to-coupling power ratios (Ω_p/Ω_c) and normalized coupling strength Ω_c/Ω_c^S result in only minimal sensitivity degradation. This intrinsic tolerance substantially relaxes experimental implementation constraints, making sub-nanovolt sensitivity achievable under realistic conditions.

ACKNOWLEDGMENTS

This work was supported by the National Natural Science Foundation of China (Grant NO. 12304545 and 12475042) and the National Key Research and Development Program of China (Grant NO. 2023YFF0718400). The authors acknowledge the use of AI-powered language editing tools to enhance the readability and grammatical accuracy of this manuscript while preserving scientific rigor and technical terminology.

DATA AVAILABILITY STATEMENT

The data that support the findings of this article are openly available [63].

-
- [1] M. Saffman, T. G. Walker, and K. Mølmer, Quantum information with rydberg atoms, *Rev. Mod. Phys.* **82**, 2313 (2010).
- [2] A. Omran, H. Levine, A. Keesling, G. Semeghini, T. T. Wang, S. Ebadi, H. Bernien, A. S. Zibrov, H. Pichler, S. Choi, J. Cui, M. Rossignolo, P. Rembold, S. Montangero, T. Calarco, M. Endres, M. Greiner, V. Vuletić, and M. D. Lukin, Generation and manipulation of schrödinger cat states in rydberg atom arrays, *Science* **365**, 570 (2019).
- [3] A. Browaeys and T. Lahaye, Many-body physics with individually controlled rydberg atoms, *Nat. Phys.* **16**, 132 (2020).
- [4] S. Ebadi, A. Keesling, M. Cain, T. T. Wang, H. Levine, D. Bluvstein, G. Semeghini, A. Omran, J.-G. Liu, R. Samajdar, X.-Z. Luo, B. Nash, X. Gao, B. Barak, E. Farhi, S. Sachdev, N. Gemelke, L. Zhou, S. Choi, H. Pichler, S.-T. Wang, M. Greiner, V. Vuletić, and M. D. Lukin, Quantum optimization of maximum independent set using rydberg atom arrays, *Science* **376**, 1209 (2022).
- [5] H. Zhang, Y. Ma, K. Liao, W. Yang, Z. Liu, D. Ding, H. Yan, W. Li, and L. Zhang, Rydberg atom electric field sensing for metrology, communication and hybrid quantum systems, *Sci. Bull.* **69**, 1515 (2024).
- [6] B. Wu, J. Yao, F. Wu, Q. An, and Y. Fu, Dependence of rydberg-atom-based sensor performance on different rydberg atom populations in one atomic-vapor cell, *Chin. Phys. B* **33**, 024205 (2024).
- [7] C. S. Adams, J. D. Pritchard, and J. P. Shaffer, Rydberg atom quantum technologies, *J. Phys. B: At. Mol. Opt. Phys.* **53**, 012002 (2019).
- [8] A. Artusio-Glimpse, M. T. Simons, N. Prajapati, and C. L. Holloway, Modern RF measurements with hot atoms: A technology review of Rydberg atom-based radio frequency field sensors, *IEEE Microw. Mag.* **23**, 44 (2022).
- [9] J. A. Sedlacek, A. Schwettmann, H. Kübler, R. Löw, T. Pfau, and J. P. Shaffer, Microwave electrometry with Rydberg atoms in a vapour cell using bright atomic resonances, *Nat. Phys.* **8**, 819 (2012).
- [10] J. A. Sedlacek, A. Schwettmann, H. Kübler, and J. P. Shaffer, Atom-based vector microwave electrometry using Rubidium Rydberg atoms in a vapor cell, *Phys. Rev. Lett.* **111**, 063001 (2013).
- [11] C. L. Holloway, J. A. Gordon, S. Jefferts, A. Schwarzkopf, D. A. Anderson, S. A. Miller, N. Thaicharoen, and G. Raithel, Broadband rydberg atom-based electric-field probe for si-traceable, self-calibrated measurements, *IEEE Trans. Antennas Propag.* **62**, 6169 (2014).
- [12] H. Fan, S. Kumar, J. Sedlacek, H. Kübler, S. Karimkashi, and J. P. Shaffer, Atom based RF electric field sensing, *J. Phys. B: At. Mol. Opt. Phys.* **48**, 202001 (2015).
- [13] M. T. Simons, A. H. Haddab, J. A. Gordon, and C. L. Holloway, A rydberg atom-based mixer: Measuring the phase of a radio frequency wave, *Appl. Phys. Lett.* **114**, 114101 (2019).
- [14] A. K. Robinson, N. Prajapati, D. Senic, M. T. Simons, and C. L. Holloway, Determining the angle-of-arrival of a radio-frequency source with a Rydberg atom-based sensor, *Appl. Phys. Lett.* **118**, 114001 (2021).
- [15] J. Hu, H. Li, R. Song, J. Bai, Y. Jiao, J. Zhao, and S. Jia, Continuously tunable radio frequency electrometry with rydberg atoms, *Appl. Phys. Lett.* **121**, 014002 (2022).
- [16] S. M. Bohaichuk, D. Booth, K. Nickerson, H. Tai, and J. P. Shaffer, Origins of Rydberg-atom electrometer transient response and its impact on radio-frequency pulse sensing, *Phys. Rev. Appl.* **18**, 034030 (2022).
- [17] S. Kumar, H. Fan, H. Kübler, J. Sheng, and J. P. Shaffer, Atom-based sensing of weak radio frequency electric fields using homodyne readout, *Sci. Rep.* **7**, 42981 (2017).
- [18] S. Kumar, H. Fan, H. Kübler, A. J. Jahangiri, and J. P. Shaffer, Rydberg-atom based radio-frequency electrometry using frequency modulation spectroscopy in room temperature vapor cells, *Opt. Express* **25**, 8625 (2017).
- [19] M. Jing, Y. Hu, J. Ma, H. Zhang, L. Zhang, L. Xiao, and S. Jia, Atomic superheterodyne receiver based on microwave-dressed Rydberg spectroscopy, *Nat. Phys.* **16**, 911 (2020).
- [20] H.-T. Tu, K.-Y. Liao, H.-L. Wang, Y.-F. Zhu, S.-Y. Qiu, H. Jiang, W. Huang, W. Bian, H. Yan, and S.-L. Zhu, Approaching the standard quantum limit of a Rydberg-atom microwave electrometer, *Sci. Adv.* **10**, eads0683 (2024).
- [21] D.-S. Ding, Z.-K. Liu, B.-S. Shi, G.-C. Guo, K. Mølmer, and C. S. Adams, Enhanced metrology at the critical point of a many-body Rydberg atomic system, *Nat. Phys.* **18**, 1447 (2022).
- [22] B. Liu, L.-H. Zhang, Q.-F. Wang, Y. Ma, T.-Y. Han, Z.-K. Liu, Z.-Y. Zhang, S.-Y. Shao, J. Zhang, Q. Li, H.-C. Chen, Y.-L. Han, D.-S. Ding, and B.-S. Shi, Cavity-enhanced Rydberg atom microwave receiver, *Chin. Phys. Lett.* **42**, 053201 (2025).
- [23] Y. Liang, Q. Wang, Z. Wang, S. Guan, P. Yang, Y. Zhang, J. He, P. Zhang, G. Li, and T. Zhang, Cavity-enhanced Rydberg atomic superheterodyne receiver, *Opt. Express* **33**, 13034 (2025).
- [24] Q. Wang, Y. Liang, Z. Wang, S. Guan, P. Yang, P. Zhang, G. Li, and T. Zhang, High-precision measurement of microwave electric field by cavity-enhanced critical behavior in a many-body Rydberg atomic system, *Sci. China-Phys. Mech. Astron.* **68**, 1 (2025).
- [25] C. L. Degen, F. Reinhard, and P. Cappellaro, Quantum sensing, *Rev. Mod. Phys.* **89**, 035002 (2017).
- [26] S. L. Braunstein and C. M. Caves, Statistical distance and the geometry of quantum states, *Phys. Rev. Lett.* **72**, 3439 (1994).
- [27] D. Spehner and M. Orszag, Geometric quantum discord with bures distance, *New J. Phys.* **15**, 103001 (2013).
- [28] M. G. Paris, Quantum estimation for quantum technology, *Int. J. Quantum Inf.* **7**, 125 (2009).

